Can a $PbCrO_4$ Photoanode Perform as Well as Isoelectronic $BiVO_4$?

Ann E. Lindberg,[1,#] Wennie Wang,[2,#] Shenli Zhang,[2] Giulia Galli,[2,3,4,*] and Kyoung-Shin Choi[1,*]

[1]*Department of Chemistry, University of Wisconsin-Madison, Madison, WI 53706, United States*

[2]*Pritker School of Molecular Engineering, University of Chicago, Chicago, IL 60637, USA*

[3]*Department of Chemistry, University of Chicago, Chicago, IL 60637, USA*

[4]*Argonne National Laboratory, Lemont, IL 60439, USA*

[#] These authors contributed equally.

* Correspondence and requests for materials should be addressed to G.G. (email: gagalli@uchicago.edu) and K.-S.C. (email: kschoi@chem.wisc.edu).

KEYWORDS: $PbCrO_4$, $BiVO_4$, photoanode, photoelectrochemical cell, solar water splitting, solar water oxidation

Abstract

Oxide-based photoelectrodes recently have been at the forefront of research for photoelectrochemical water splitting. While most oxide-based photoanodes suffer from severe electron-hole recombination, $BiVO_4$ photoanodes are known to achieve exceptionally high electron-hole separation efficiencies. However, an understanding of what features of $BiVO_4$ lead to this desired property is currently lacking. In this study, we sought to elucidate these features by investigating $PbCrO_4$, which has electronic and structural similarities to $BiVO_4$. For this goal, we prepared $PbCrO_4$ as a high-quality photoanode and compared its photoelectrochemical properties and stability with those of $BiVO_4$. Our results showed that the electron-hole separation efficiency for $PbCrO_4$ at 1.23 V vs RHE was ~67%, which is considerably higher than most oxide photoanodes and approaches that of state-of-the-art $BiVO_4$. The photoelectrochemical similarities and differences between $PbCrO_4$ and $BiVO_4$ were discussed in detail, and the origins for their similarities and differences were investigated via combined experimental and computational studies, which include the computation of electronic band structures, band edge alignments, and the formation energies of oxygen vacancies of $PbCrO_4$ and $BiVO_4$. The shared electronic and structural features of $PbCrO_4$ and $BiVO_4$ elucidated in this study provide useful guidelines to develop high-performance oxide-based photoanodes.

1. Introduction

Solar water splitting using photoelectrochemical cells (PECs) can offer a promising route to producing hydrogen as a clean fuel in an environmentally benign way.[1–3] Oxide-based photoelectrodes are appealing for use in PECs due to their inexpensive and facile processing as well as their relatively high stabilities in aqueous media.[3] However, oxide-based photoelectrodes are typically known to suffer from high electron-hole recombination and therefore cannot efficiently utilize photogenerated charge carriers. For example, the electron-hole separation yields of most oxide-based photoanodes are lower than 10% at 1.23 V vs the reversible hydrogen electrode (RHE).[3]

$BiVO_4$ is exceptional in that its electron-hole separation yield reaches almost 100% at 1.23 V vs RHE and exceeds 70% even at 0.6 V vs RHE.[3–6] Therefore, although its bandgap is relatively large (2.4-2.6 eV)[7–12], $BiVO_4$ generates significantly higher photocurrent than photoanodes with smaller bandgaps that suffer from poor electron-hole separation. Another attractive feature of $BiVO_4$ is its conduction band minimum (CBM), which is located very close to the water reduction potential. As a result, it is possible to produce $BiVO_4$ with a flatband potential (E_{FB}) close to 0.1 V vs RHE.[3,4] Furthermore, $BiVO_4$ does not suffer from extremely fast surface recombination; therefore, the difference between its E_{FB} and its photocurrent onset potential for water reduction can be within 10 mV when it is paired with an oxygen evolution catalyst.[3,4,6,13,14] As a result, $BiVO_4$ can achieve a photovoltage for water oxidation (defined as the difference between the photocurrent onset potential and the thermodynamic water oxidation potential) greater than 1 V.[3,4,6,13,14]

The fact that $BiVO_4$ can achieve a high electron-hole separation yield and photovoltage for water oxidation encourages further investigation of the development of more efficient oxide-based photoelectrodes. However, it is not clear what features of $BiVO_4$ make its photoelectrochemical

properties so remarkably different from those of other oxide photoanodes. Elucidating these features may lead to the more effective development of oxide photoelectrodes that have the advantageous features of $BiVO_4$ but a smaller bandgap.

In an effort to understand the beneficial features of $BiVO_4$, we investigated the photoelectrochemical properties of $PbCrO_4$ in this study. $PbCrO_4$ is the compound that most closely mimics the composition and electronic structure of $BiVO_4$. Pb is located to the left of Bi in the 6th row of the periodic table; therefore, Pb^{2+} and Bi^{3+} are isoelectronic and both contain filled 6s orbitals. Cr is located to the right of V in the 4th row of the periodic table, so Cr^{6+} and V^{5+} are isoelectronic and both contain unfilled 3d orbitals. $BiVO_4$ and $PbCrO_4$, however, are not isostructural and possess slightly different crystal structures (**Figure 1**). $BiVO_4$ has a scheelite-type structure in which each V ion is coordinated by four O atoms in a tetrahedral site and each Bi ion is coordinated by eight O atoms from eight different VO_4 tetrahedral units.[15] The Bi polyhedra form the 3D framework through edge-sharing with four other Bi polyhedra. The VO_4 tetrahedra are not connected to other VO_4 tetrahedra and are attached to the Bi polyhedral chain through corner sharing. $PbCrO_4$ has a monazite-type structure in which each Cr is coordinated by four O atoms in a tetrahedral site and each Pb ion is coordinated by nine O atoms.[16] The Pb polyhedra form the 3D framework through edge-sharing with six other Pb polyhedra. The CrO_4 tetrahedra are not connected to other CrO_4 tetrahedra. Instead, each CrO_4 tetrahedron is connected to six Pb polyhedra, two through edge-sharing and four through corner sharing.

Although the structures of $BiVO_4$ and $PbCrO_4$ are not the same, they still share many structural features. First, the three-dimensional framework is made only through main group metal polyhedra, and the transition metal polyhedra do not form an extended network. Second, within each compound, the local environments of the main group metal ion and the transition metal ion

are substantially different from each other (8- or 9-coordinated polyhedra for the main group metal and 4-coordinated tetrahedra for the transition metal ion), which may result in a low probability for the two metal ions to swap positions and create defects. Therefore, it is interesting and informative to investigate whether $PbCrO_4$ can achieve an electron-hole separation yield as high as $BiVO_4$. If it does, the common electronic and structural features of $BiVO_4$ and $PbCrO_4$ can offer guidelines to design oxide photoelectrodes to achieve high electron-hole separation yields. If $PbCrO_4$ does not have a high electron-hole separation yield, then it means that the identities of the metals and the structural differences of the bulk and/or surface between $BiVO_4$ and $PbCrO_4$ do play a significant role in differentiating their photoelectrochemical properties.

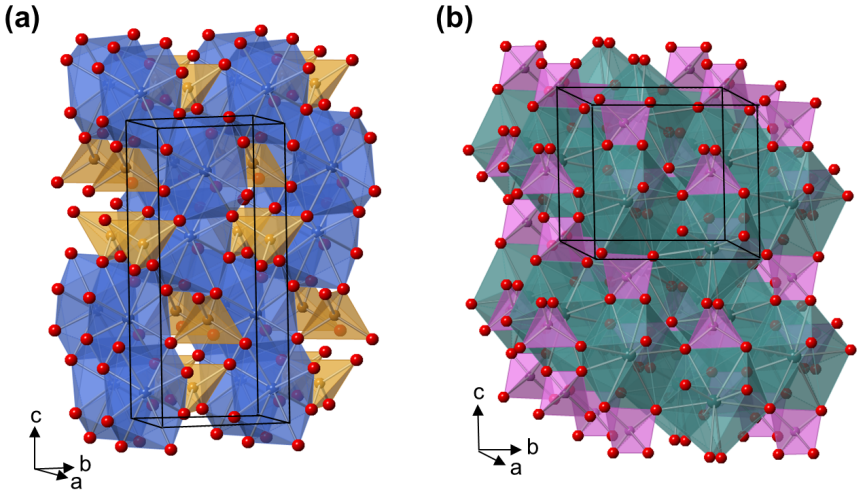

Figure 1. Crystal structures of (a) $BiVO_4$ and (b) $PbCrO_4$. Bi is blue, V is gold, Pb is green, Cr is pink, and O is red.

There have been a few previous papers on $PbCrO_4$ as a photoanode, but the photocurrent densities of $PbCrO_4$ reported in these studies were not close to those of $BiVO_4$.[17,18] For example, at 1.23 V vs RHE, the best performance achieved by $PbCrO_4$ for sulfite oxidation is 0.5 mA/cm^2, while that of $BiVO_4$ is ~5 mA/cm^2.[5,6,18] However, we note that the electron-hole separation yield

or any other photoelectrochemical property of a polycrystalline photoelectrode varies significantly depending on the quality of the photoelectrode because impurities, unevenness in composition, poor electrical continuity, poor quality interface with the conducting substrate, and poor crystallinity considerably affect the electron-hole recombination and charge transport properties. The morphology of the photoelectrode also plays a significant role in affecting its photoelectrochemical properties. Thus, a high-quality $PbCrO_4$ photoanode needs to be prepared first for a fair comparison. Even for $BiVO_4$, extensive effort was necessary to prepare high-quality photoelectrodes before its exceptional photoelectrochemical properties were observed.[3,4,8,19]

In this study, we prepared a pure, high-quality $PbCrO_4$ photoanode and examined its photoelectrochemical properties. The toxicity of Pb and Cr makes the practical application of $PbCrO_4$ as a photoanode unlikely. However, we note that the purpose of the current study is not to develop $PbCrO_4$ as a practical photoanode but to elucidate the factors that are responsible for the exceptional features of $BiVO_4$ by comparing it to $PbCrO_4$. The outcome of this study will provide unique and interesting insights into the features defining efficient oxide photoanodes.

2. Experimental

Materials. Lead (II) nitrate ($Pb(NO_3)_2$, 99%) was purchased from Fluka. Chromium (III) nitrate nonahydrate ($Cr(NO_3)_3 \cdot 9H_2O$, 99%) and N,N-dimethylformamide ($HCON(CH_3)_2$, ≥99.8%) were purchased from Sigma-Aldrich. Boric acid (H_3BO_3, >99%) was purchased from Alfa Aesar for buffer solutions. Sodium sulfite (Na_2SO_3, 98%) was purchased from Sigma-Aldrich for photocurrent measurements as a hole scavenger. Hydrogen peroxide (H_2O_2, 30% solution (w/v)) was purchased from EMD Millipore Corporation for use as a hole scavenger. All chemicals were

used as purchased without further purification. All solutions were prepared using deionized water further purified with a Barnstead E-pure (model D4631) purification system (resistivity ≥ 18 MΩ).

Fluorine-doped tin oxide (FTO) coated glass slides (TEC15, 12-14 Ω/sq resistance, Hartford Glass) were cleaned via sonication for 15 min each in isopropyl alcohol, acetone, and E-pure water prior to use for film deposition. Platinum electrodes were prepared by sputter-coating a 100-nm Pt layer over a 20-nm Ti layer onto clean glass slides.

Synthesis of $PbCrO_4$. Electrodeposition was carried out in an undivided cell using a VMP2 multichannel potentiostat (Princeton Applied Research). A three-electrode system was used, consisting of an FTO working electrode, FTO counter electrode, and an Ag/AgCl (4 M KCl) reference electrode. The FTO working electrode was masked with Teflon tape to expose a known surface area (~1.2 cm^2).[20]

Pb metal films were cathodically deposited from a plating solution consisting of 50 mM $Pb(NO_3)_2$ in deionized water (pH 4.7). A potentiostatic deposition was performed, applying a potential of -0.8 V vs Ag/AgCl to pass 0.35 C/cm^2. The as-deposited Pb metal films were dried in air.

Conversion of the Pb metal films to $PbCrO_4$ was achieved by drop-casting 50 μL of a solution containing Cr^{3+} ions on the films and annealing to allow for a solid-state reaction between Cr and Pb. The drop-casting solution contained 45 mM $Cr(NO_3)_3 \cdot 9H_2O$ in N,N-dimethylformamide (DMF). Films were annealed in air at 500 °C for 2 h (2.64 °C/min ramp rate). This method produced pure, high-quality $PbCrO_4$ in the center of the electrode, which was dark yellow in color. However, when the Cr-containing DMF solution evaporated, the edges of the films became more concentrated in Cr than the centers of the films (a.k.a. coffee-ring effect). As a result, the edge of the electrode contained excess chromium oxide, indicated as a gray color. The presence

of the Cr-rich edge regions did not affect the characterization and photoelectrochemical properties of $PbCrO_4$ as these regions were avoided or masked for measurements. We did not further modify our synthesis to extend the purity of the samples to the edge regions because our results showed that the center of the electrode contained pure, high-quality $PbCrO_4$ that was sufficient to achieve the goal of the study, and it is not likely that $PbCrO_4$ will be used as a practical photoanode due to its toxicity.

Characterization. The purity and crystal structure of $PbCrO_4$ were examined by powder X-ray diffraction (XRD; Bruker D8 Advanced PXRD, $\lambda = 1.5418$ Å, 298 K, Ni-filtered Cu K_α radiation). The morphologies of the synthesized electrodes were examined with a scanning electron microscope (SEM; LEO Supra55 VP) operated at an accelerating voltage of 2 kV. The atomic composition of $PbCrO_4$ was measured with energy-dispersive X-ray spectroscopy (EDS) using the same SEM equipped with an EDS detector (Noran System Seven, Thermo Fisher) at an accelerating voltage of 22 kV. UV-vis absorption spectra were obtained using a Cary 5000 UV-vis-NIR spectrophotometer (Agilent), in which the sample was placed in the center of an integrating sphere to measure all reflected and transmitted light.

Photoelectrochemical and Electrochemical Characterization. The photoelectrochemical performance of $PbCrO_4$ used in this study was evaluated in an undivided three-electrode configuration using an SP-200 potentiostat/EIS (BioLogic Science Instruments). Simulated solar illumination was obtained by passing light from a 300 W Xe arc lamp (Ushio America, Inc.) through a water (IR) filter, neutral density filters, and an AM 1.5G filter into an optical fiber. $PbCrO_4$ electrodes were illuminated through the FTO (back-side illumination). The power density of the incident light was calibrated to 100 mW/cm^2 at the FTO surface (before the light passed through FTO) using an NREL-certified GaAs reference cell (Photo Emission Tech, Inc.). All

sample electrodes were masked to make the exposed geometrical area (~0.02-0.03 cm^2) smaller than the illuminated area (0.06 cm^2).

Photoelectrochemical measurements were performed in 1.0 M borate buffer at pH 9.0, with 0.1 M H_2O_2 or Na_2SO_3 as a hole scavenger. J-V performance was measured by sweeping the potential at a rate of 10 mV/s to the positive direction from the open circuit potential while chopping the light. Photoelectrochemical stability was measured by holding the potential at 1.0 V vs RHE while illuminating the electrode. All measurements were carried out using a Pt counter electrode and an Ag/AgCl reference electrode (4 M KCl). The potential was converted from Ag/AgCl to RHE using the following equation:

$$E\ (\text{vs RHE}) = E\ (\text{vs Ag/AgCl}) + E_{Ag/AgCl}\ (\text{reference}) + 0.0591\ \text{V} \times \text{pH}$$

$$(E_{Ag/AgCl}\ (\text{reference}) = 0.1976\ \text{V vs NHE at 25 °C})$$

Capacitance measurements for Mott-Schottky plots were obtained using the aforementioned three-electrode cell configuration and SP-200 potentiostat/EIS (BioLogic Science Instruments). The measurements were taken in 1.0 M borate buffer solution at pH 9.0. A sinusoidal modulation of 10 mV was applied at frequencies of 0.5, 1, and 2.5 kHz.

Incident photon-to-current efficiency (IPCE) was determined using illumination from a 300 W Xe arc lamp passed through neutral density filters and an AM 1.5G filter. Monochromatic light was produced by an Oriel Cornerstone 130 monochromator with a 10-nm bandpass. The intensity of incident light was calibrated to 100 mW/cm^2 using a silicon photodiode detector (International Light, SED033). IPCE was measured in 1.0 M borate buffer at pH 9.0 with 0.1 M H_2O_2 as a hole scavenger. The three-electrode configuration described above for photocurrent measurements was utilized, and a potential of 1 V vs RHE was applied. Absorbed photon-to-

current efficiency (APCE) was determined by dividing the IPCE by the light harvesting efficiency (LHE) using the following equations:

$$\text{APCE (\%)} = \text{IPCE (\%)}/\text{LHE}$$

$$\text{LHE} = 1 - 10^{-A(\lambda)}, \text{ where } A(\lambda) = \text{absorbance at wavelength } \lambda$$

Computational Methods. We carried out electronic structure calculations of $PbCrO_4$ using density functional theory (DFT)[21,22] and the PBE functional[23] with a Hubbard *U* parameter,[24] as implemented in QUANTUM ESPRESSO (QE, v 6.3).[25,26] Following the protocol employed in our previous work on $BiVO_4$,[27] we used norm-conserving pseudopotentials[28,29] and a kinetic energy cutoff of 90 Ry. The Pb $5d^{10}6s^26p^2$, Cr $3s^23p^64s^23d^4$, and O $2s^22p^6$ electrons were treated as valence electrons. We used a cell with 24 atoms, a 5x5x5 *k*-point grid and optimized atomic coordinates until forces were smaller than 3 meV/Å. For slab calculations, we generated symmetric slabs[30] with routines from Pymatgen[31] and the Atomic Simulation Environment[32] using a minimum of 8 atomic layers and 20 Å in vacuum and relaxed internal coordinates until forces were smaller than 100 meV/Å.

The Hubbard correction *U* was applied on the Cr *d* states.[24] We performed calculations using two values of *U: U* = 2.7 eV, i.e., the same value adopted in our previous calculations of the (010) $BiVO_4$ surface,[27] and *U* = 3.7 eV, which covers the range of values of *U* used in the literature and was determined based on the study of embedded clusters of chromia (*U* = 3.2 eV)[33] and the oxidation energy of chromia (*U* = 3.5 – 3.7 eV).[34,35]

Using supercells, we computed the formation energy of a neutral oxygen vacancy[36] and assumed the O-rich limit in our calculations. We used a 3x2x2 (288-atom) supercell for $PbCrO_4$ and calculated total energies using the Γ-point to sample the Brillouin zone.

A detailed account on the surface electronic properties of the (010) $BiVO_4$ surface with and without oxygen vacancies using the same computational methodology has been published in our previous paper.[27] In order for the readers to directly compare the results of $PbCrO_4$ and $BiVO_4$ side by side, some of the $BiVO_4$ results are reproduced in this study and presented with the new results obtained for $PbCrO_4$.

3. Results and Discussion

3-1. Experimental Study

The $PbCrO_4$ electrode used in this study was prepared by a two-step process. The first step was the electrodeposition of Pb metal precursor films, which was achieved through reduction of Pb^{2+} to Pb^0 in a plating solution containing $Pb(NO_3)_2$. Pb metal was first deposited as a thin film over the FTO substrate. Once the FTO substrate was covered by the Pb layer, Pb was deposited as micron-sized crystals on top (**Figure 2a, b**). The x-ray diffraction (XRD) pattern of the as-deposited films showed highly crystalline Pb peaks with no impurities or oxide peaks present (**Figure 3a**). The second step was the conversion of Pb metal to $PbCrO_4$, which was achieved by annealing the precursor films with a DMF solution containing $Cr(NO_3)_3 \cdot 9\ H_2O$ as the chromium source in air for 2 hours at 500 °C.

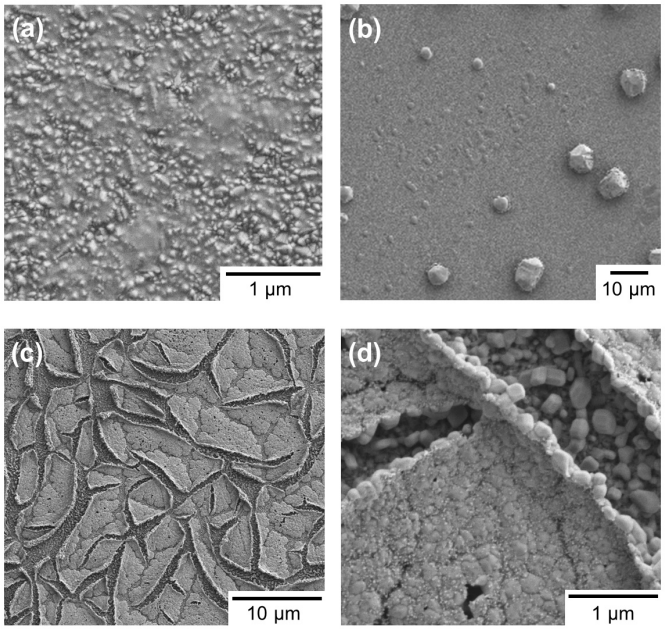

Figure 2. (a) High- and (b) low-magnification SEM images of as-deposited Pb metal. (c) Low- and (d) high-magnification SEM images of $PbCrO_4$.

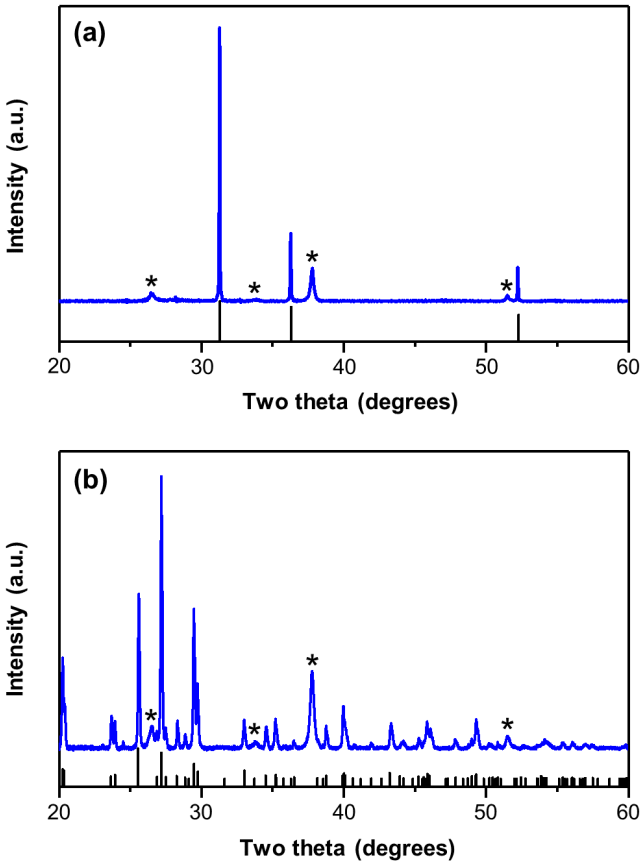

Figure 3. XRD pattern of (a) as-deposited Pb metal. Vertical black lines correspond to the calculated diffraction pattern for cubic Pb (PDF No. 00-004-0686). FTO substrate peaks are marked with an asterisk. (b) XRD pattern of $PbCrO_4$. Vertical black lines correspond to calculated diffraction pattern for monoclinic $PbCrO_4$ (PDF No. 01-074-2304). FTO substrate peaks are marked with an asterisk.

The final $PbCrO_4$ films showed a markedly different morphology than the precursor film (**Figure 2c**). This is due to the low melting point of lead (327.5 °C) as well as the formation of a new phase, $PbCrO_4$. This new morphology was composed of islands of close-packed particles with an average grain size of several hundred nanometers (~100-200 nm) across. Each island is ~250 nm thick (**Figure S1**). Large cracks between islands were observed, which revealed areas where the FTO was covered by individual particles of $PbCrO_4$ (**Figure 2d**). Highly crystalline peaks were observed via XRD (**Figure 3b**) that matched the calculated diffraction pattern for $PbCrO_4$, and the absence of other lead chromate phases (Pb_2CrO_5 and Pb_5CrO_8) was carefully confirmed. EDS of the $PbCrO_4$ film verified a Pb:Cr ratio of 1:1.

The UV-vis absorption spectrum of $PbCrO_4$ is shown in **Figure 4a** in comparison with the spectrum of nanoporous $BiVO_4$ films synthesized using a method developed previously in our group.[6] The maximum absorbance of the $PbCrO_4$ electrode is lower than the well-optimized, much thicker, nanoporous $BiVO_4$. However, the absorption onset for $PbCrO_4$ was as sharp as that of $BiVO_4$. Also, $PbCrO_4$ has a smaller bandgap (~2.3 eV) than that of BiVO4 (~2.5 eV). The measured $PbCrO_4$ bandgap matches those reported previously in the literature.[17,18,37]

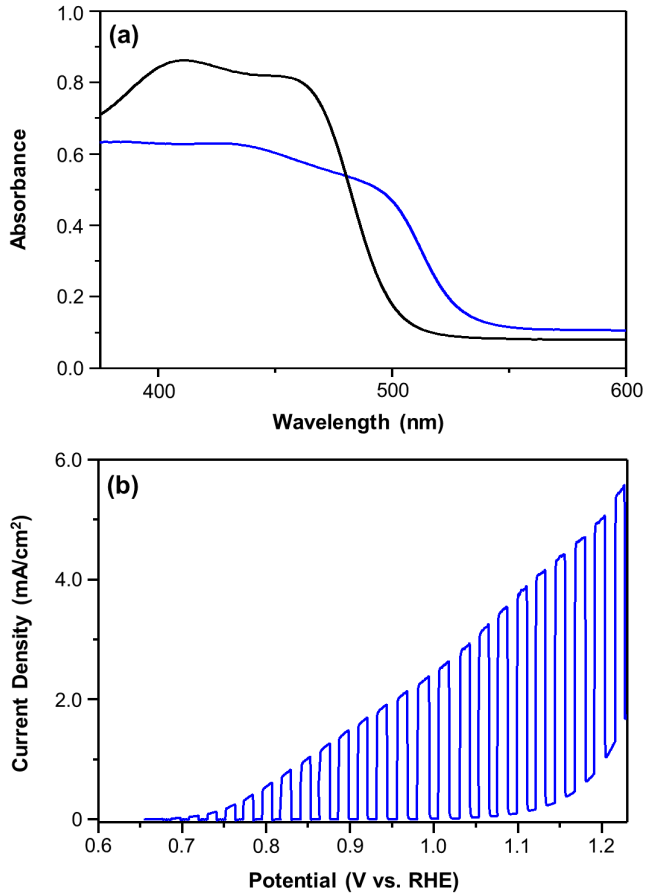

Figure 4. (a) UV-vis absorbance of $PbCrO_4$ (blue) and nanoporous $BiVO_4$ (black) and (b) J-V plot for H_2O_2 oxidation. Measurement was performed in pH 9.0 borate buffer containing 0.1 M H_2O_2 using AM 1.5G (100 mW/cm^2) illumination.

The photoelectrochemical behavior of $PbCrO_4$ was first investigated in pH 9 borate buffer with 0.1 M Na_2SO_3 as the hole scavenger. The rapid oxidation kinetics of a hole scavenger such as sulfite allows us to assume that the loss of surface-reaching holes to surface recombination is negligible.[20] Thus, the photocurrent measured for oxidation of a hole scavenger can provide a good estimation of the bulk electron-hole separation yield, which will be explained in detail below. Unfortunately, we found that $PbCrO_4$ is not chemically stable in sulfite solution and is converted to $PbSO_3$ over time (**Figure S2**). This conversion was expedited when $PbCrO_4$ was illuminated for

photocurrent measurement in the sulfite solution (**Figure S3**). Therefore, we concluded that sulfite is not a proper hole scavenger to examine the photoelectrochemical properties of $PbCrO_4$.

The primary alternative hole scavenger to sulfite in the literature is H_2O_2 and was thus chosen for all further photoelectrochemical characterization of $PbCrO_4$ films.[20,38,39] The chemical stability of $PbCrO_4$ in a solution of pH 9 borate buffer and 0.1 M H_2O_2 was first examined. After immersing the electrodes overnight, the morphology of the $PbCrO_4$ films did not change, and EDS confirmed no change in elemental composition. The J–V plot in pH 9 borate buffer with 0.1 M H_2O_2 under AM 1.5G, 100 mW/cm^2 illumination is shown in **Figure 4b**. A photocurrent of ~3.8 mA/cm^2 was observed at 1.23 V vs RHE. This current density is the highest photocurrent observed with a hole scavenger for $PbCrO_4$ as well as for most ternary oxide-based photoelectrodes aside from nanoporous $BiVO_4$.[3] Additionally, this photocurrent is higher than that achieved by $BiVO_4$ with a dense morphology that was electrochemically synthesized by our group (1.8 mA/cm^2 at 1.23 V vs RHE).[19]

The electron-hole separation yield, φ_{sep}, is the fraction of photogenerated holes that are transported to the electrode surface. The φ_{sep} for $PbCrO_4$ was calculated using Eq. 1,[20] where $J_{PEC(H_2O_2)}$ is the measured photocurrent density for H_2O_2 oxidation, J_{abs} is the current density assuming 100% absorbed photon-to-current efficiency (APCE), and φ_{ox} is the charge injection yield indicative of the fraction of surface-reaching holes that are injected into the solution species. For a hole scavenger like H_2O_2, φ_{ox} can be assumed to be ~1. (We note that this assumption is valid only when the photoelectrode does not suffer from extremely fast surface recombination that is even faster than hole injection to H_2O_2.)

$$J_{PEC(H_2O_2)} = J_{abs} \times \varphi_{sep} \times \varphi_{ox} \qquad \text{Eq. 1}$$

J_{abs} of the $PbCrO_4$ electrode was calculated to be 5.7 mA/cm^2. This value was determined by multiplying the number of photons in the AM 1.5G spectrum at each wavelength by the light harvesting efficiency of $PbCrO_4$ at each wavelength. Then, a trapezoidal integration in 10-nm increments was used to calculate the total number of photons absorbed by $PbCrO_4$, which was subsequently converted to current density assuming 100% APCE. The calculated φ_{sep} was ~67% at 1.23 V vs RHE. This is a higher value than the φ_{sep} of thin $BiVO_4$ with a similar morphology (~50%) but lower than the 90% that was reported for nanoporous $BiVO_4$, which has an improved φ_{sep} due to nanostructuring.[4,19]

The photocurrent onset of the $PbCrO_4$ film occurred at ~0.67 V vs RHE (**Figure 4b**), which is much more positive than the photocurrent onset for $BiVO_4$ (~0.2 V vs RHE).[3,4] The photocurrent onset potential obtained with a hole scavenger is equivalent to the E_{FB} of the photoanode unless the photoanode suffers from extremely fast surface recombination that is even faster than the oxidation kinetics of the hole scavenger. The E_{FB} of $PbCrO_4$ was additionally determined by Mott-Schottky analysis. A slight frequency dependence was observed for the plots obtained for three different frequencies, but the E_{FB} was reasonably estimated to be ~0.62 V vs RHE, which is within 50 mV from the photocurrent onset observed in the J-V measurements (**Figure S4**).

We note that both the CBM and carrier density affect the E_{FB}. Therefore, from the J-V plot alone, it is difficult to judge whether the considerably more positive E_{FB} of $PbCrO_4$ compared with that of $BiVO_4$ is due to the considerably more positive CBM or lower carrier density of the $PbCrO_4$ used in this study. The computational study on the electronic structure of $PbCrO_4$ discussed below shows that the CBM of $PbCrO_4$ is a few hundred mV more positive (i.e., farther from vacuum) than that of $BiVO_4$, and the calculated oxygen vacancy formation energy indicates that the carrier density in $PbCrO_4$ is unlikely lower than that in $BiVO_4$. Thus, we believe that the more positive

E_{FB} of $PbCrO_4$ shown in this study is due to the CBM position of $PbCrO_4$, which intrinsically limits the E_{FB}.

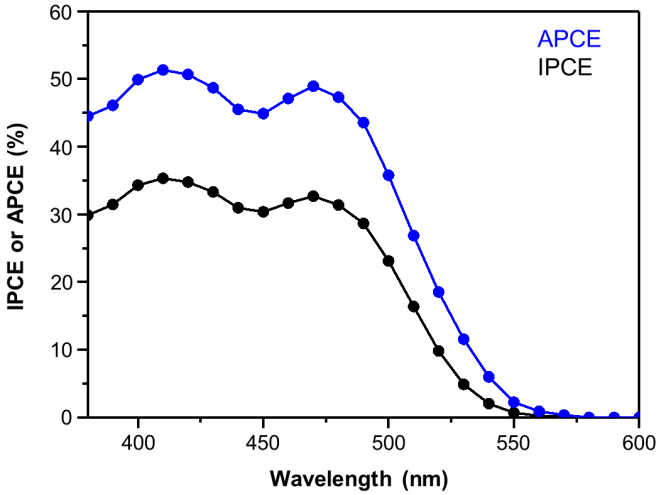

Figure 5. IPCE (black) and APCE (blue) for $PbCrO_4$ measured for H_2O_2 oxidation at 1.0 V vs RHE. Measurement was performed in pH 9.0 borate buffer containing 0.1 M H_2O_2.

Incident photon-to-current efficiency (IPCE) and APCE measurements were performed to additionally assess the material's efficiency with regards to photon absorption and bulk electron-hole separation.[20,40] IPCE was measured in a solution of pH 9 borate buffer and 0.1 M H_2O_2 at an applied potential of 1.0 V vs RHE. (This potential was chosen because the electrochemical oxidation of H_2O_2 occurs at 1.05 V vs RHE.) The IPCE reaches a maximum of 35% at 410 nm with an APCE of 51% (**Figure 5**). These values are considerably higher than those reported for most metal oxides photoelectrodes. Our results suggest that like $BiVO_4$, $PbCrO_4$ also does not suffer from severe electron-hole recombination.

J-t measurements at 1.0 V vs RHE with H_2O_2 as the hole scavenger (**Figure S5a**) showed a decay in the photocurrent density to zero over one hour. Characterization of these films showed etching and dissolution of the film (**Figure S5b**) with a final Pb:Cr ratio of 0.5:1 by EDS. These results show that $PbCrO_4$ is photoelectrochemically unstable. For comparison, $BiVO_4$ is stable for

photoelectrochemical sulfite oxidation in a pH ~9 solution.[6] These results show that even for isoelectronic photoelectrodes with similar structures, their photoelectrochemical stabilities can be different depending on the redox chemistry and solubility of the individual constituent metal ions (e.g. Pb^{2+} and Bi^{3+}).

Although the goal of the study is to investigate the electron-hole separation and not the water oxidation performance of $PbCrO_4$, the J-V and J-t plots of $PbCrO_4$ obtained in pH 9.0 borate buffer are shown in **Figure S6**.

3-2. Computational Study

We used first-principles calculations to examine the bandgap and band alignments of the bulk and surface of $PbCrO_4$. We compared our results with those previously obtained for $BiVO_4$ in our recent study,[27] where we found good agreement with measured band alignments and work functions and showed that the methodology used was robust. We primarily compared results for $PbCrO_4$ to $BiVO_4$ obtained using U = 2.7 eV and note that increasing U to 3.7 eV results in less than 0.1% change in the lattice parameter, less than 0.002 Å change in bond lengths, less than 1% change in bandgap, and less than 1% change in band position with respect to the vacuum. Our calculated lattice parameters for $PbCrO_4$ are a = 7.29 Å, b = 7.60 Å, c = 6.90 Å, and β=102.91°, which are in good agreement with previous reports.[17,35,41,42] The calculated bandgap is 2.05 eV, which is a slight underestimation compared to the measured one (~ 2.25 eV).[17,41] We note that the calculated bandgap of $BiVO_4$ (2.27 eV)[27] is similarly underestimated compared to measurements.[8–12] Nevertheless, the difference in the bandgap of the two materials is consistent with that obtained from UV-vis absorbance in **Figure 4**; hence, we expect our calculations to predict the correct relative band alignment between the two oxides.

Figure 6 shows the bulk electronic structures of $PbCrO_4$ and $BiVO_4$ along a high-symmetry *k*-point path chosen following the conventions of Ref. 43. Similar to the atomic structure, the electronic structures of these ABO_4 (where A = Pb or Bi and B = Cr or V) transition metal oxides share many similarities. The electronic states near the valence band maxima (VBMs) are composed of primarily O 2*p* states with a sizeable contribution from the A-site metal 6*s* states, which are known to correspond to electron lone pairs.[44,45] The conduction band states are primarily composed of the B-site metal 3*d* states with appreciable O 2*p* character and some A-site metal 6*p* character. The 3*d* states of Cr are lower in energy than those of V, and as a consequence, the CBM of $PbCrO_4$ is lower, resulting in its smaller bandgap.

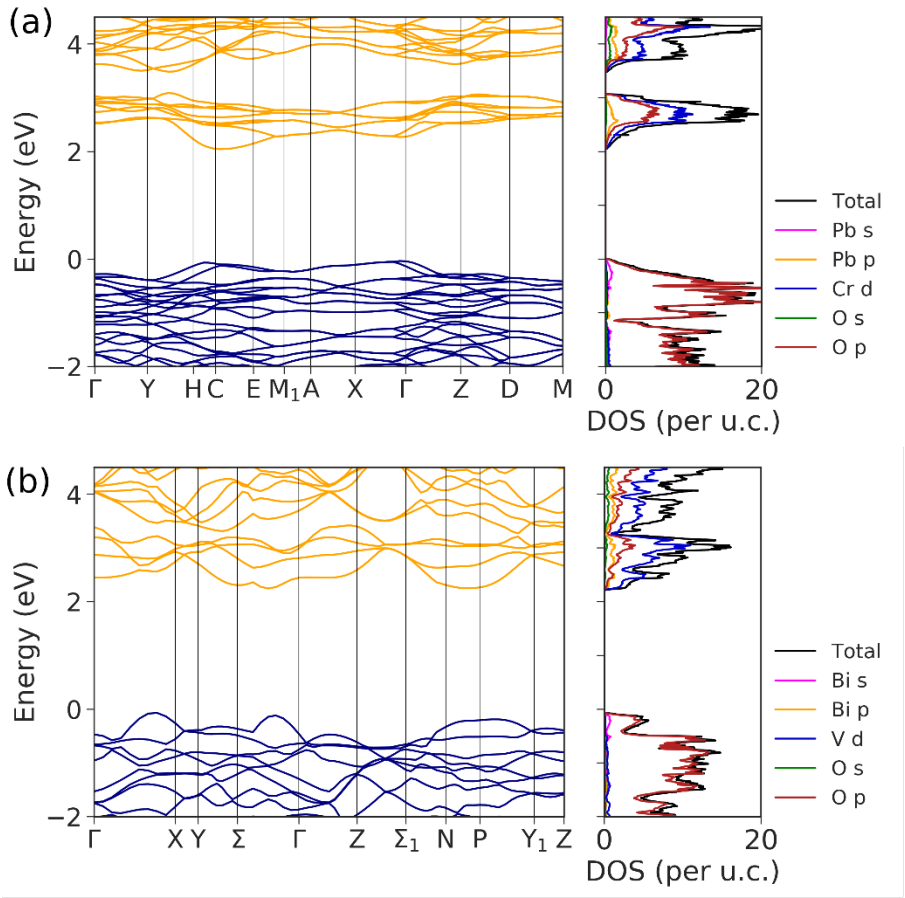

Figure 6. Band structure and corresponding density of states for (a) $PbCrO_4$ and (b) $BiVO_4$. Valence bands are shown in blue, and conduction bands are shown in orange. The zero of energy

is taken as the VBM, and the high-symmetry *k*-point path chosen here follows the convention of Ref. 43. The right panel of Figure 6b is adapted from Ref. 27. Copyright 2020 American Chemical Society.

In order to elucidate the trends observed in the photoelectrochemical measurements, we compared band alignments of $PbCrO_4$ and $BiVO_4$. We first performed a search for the low-energy structure of low-index surfaces. Slab structures of $PbCrO_4$ were selected such that they exhibit similar features to the (010) surface of $BiVO_4$; specifically, the surface B-site metal is 4-fold coordinated and the surface A:B ratio is 1:1. (The Miller indices of $BiVO_4$ were based on the monoclinic C 2/c cell.) We found that the (010) and (100) surfaces of $PbCrO_4$ (based on the monoclinic P 2_1/n cell) have comparable surface energies (within 0.01 J/m^2 of each other and (100) being lower); they are shown in **Figure 7a** along with the surface structure of the (010) $BiVO_4$ surface for comparison. Both the (010) and (100) surfaces of $PbCrO_4$ have 6-fold and 7-fold coordinated surface Pb, whereas the $BiVO_4$ (010) surface has only 6-fold coordinated surface Bi.

Figure 7b presents the absolute band alignments with respect to the vacuum level for the two surfaces of $PbCrO_4$ shown in **Figure 7a**. The calculated[27] and measured[9] band alignments for the $BiVO_4$ surface are presented for comparison and show good agreement with each other. Our calculations show that the VBM of $PbCrO_4$ is similar to that of $BiVO_4$ (within ~ 0.1 eV); however, the CBM positions differ. The CBM of $PbCrO_4$ is 0.31 eV and 0.48 eV below that of $BiVO_4$ for the (010) and (100) surfaces, respectively. As a result, the bandgap of the $PbCrO_4$ slab is ~1.9 eV, smaller than that of $BiVO_4$ (~2.25 eV). We note that the surface bandgap is very similar to the bulk bandgap in the case of $BiVO_4$, but it is slightly smaller in the case of $PbCrO_4$. We further note that the difference in band edge positions between the $PbCrO_4$ (010) and (100) surfaces originates from the difference in the average electrostatic potential of the different surfaces.[46,47]

We next compare our calculated band offsets with the experimentally observed E_{FB} values of $PbCrO_4$ and $BiVO_4$. As mentioned earlier, the E_{FB} of $PbCrO_4$, determined by its photocurrent onset for sulfite oxidation and Mott-Schottky plots, was 0.4 - 0.5 V more positive than that reported for $BiVO_4$. The fact that the computed CBM of $PbCrO_4$ is lower than that of $BiVO_4$ by 0.31 - 0.48 eV suggests that the difference in the E_{FB} is largely attributable to the difference in the CBM of $PbCrO_4$ and $BiVO_4$.

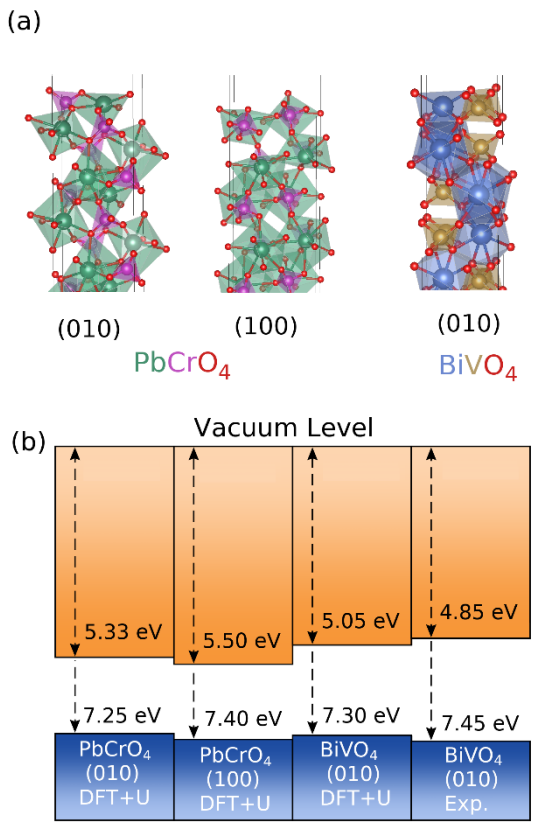

Figure 7. (a) Slab structures adopted in our calculations for the (010) and (100) surfaces of $PbCrO_4$ alongside the (010) surface for $BiVO_4$. Pb atoms are shown in green, Cr atoms in pink, Bi atoms in blue, V atoms in gold, and O atoms in red. (b) Band alignments for the (010) and (100) surfaces of $PbCrO_4$ compared to that of the (010) surface of $BiVO_4$,[27] all of which were calculated using DFT+U= 2.7 eV. For reference, we also give the measured band alignment of the (010) surface for a single-crystalline sample of $BiVO_4$.[9] The band alignment plot was generated with the help of bapt (https://github.com/utf/bapt). The portion related $BiVO_4$ in Figure 7b is adapted from Ref. 27. Copyright 2020 American Chemical Society.

Finally, we compared the neutral oxygen vacancy formation energy in the bulk of $PbCrO_4$ and $BiVO_4$ to compare their tendencies to form oxygen vacancies as intrinsic defects. For $PbCrO_4$ and $BiVO_4$ with no extrinsic dopants, oxygen vacancies are the major defect responsible for their n-type nature. As reported by Seo *et al.* for $BiVO_4$,[48] the VO_3 polyhedron with a missing oxygen is distorted and has a configuration where it shares a corner with a neighboring VO_4 tetrahedron. Multiple electronic structure configurations for the two excess electrons associated with the neutral oxygen vacancy are possible, depending on whether the electrons form polarons localized on the VO_3 or on a neighboring VO_4 polyhedron. Using a 216-atom supercell, Seo *et al.* determined the formation energy of a neutral oxygen vacancy for the lowest energy configuration in the bulk of $BiVO_4$ to be 2.75 eV.[48]

Due to the structural similarities between $PbCrO_4$ and $BiVO_4$, we initialized our 288-atom supercell for $PbCrO_4$ to be in a similar configuration as the lowest energy one found in $BiVO_4$. Interestingly, unlike the VO_3 polyhedron in $BiVO_4$, the CrO_3 polyhedron does not distort to share a corner with a neighboring CrO_4 tetrahedron. Instead, both CrO_3 and CrO_4 polyhedra relax back to their positions in the pristine bulk. Our calculated formation energy for the neutral oxygen vacancy in $PbCrO_4$ is 2.37 eV, which is lower than that of $BiVO_4$, indicating that $PbCrO_4$ is likely to have a higher concentration of oxygen vacancies in thermodynamic equilibrium. Therefore, if we assume that the oxygen vacancies in $BiVO_4$ and $PbCrO_4$ have comparable ionization energies as donors, this result suggests that the carrier density of $PbCrO_4$ should not be considerably lower than that of $BiVO_4$, and it cannot be the reason for the more positive E_{FB} of $PbCrO_4$. Thus, this result additionally confirms that the more positive E_{FB} of $PbCrO_4$ is due to its CBM being considerably more positive (i.e., farther from vacuum) than that of $BiVO_4$.

4. Conclusions

In this study, we compared photoelectrochemical properties, electronic band structures, and band alignments of $PbCrO_4$ and $BiVO_4$ to examine whether a $PbCrO_4$ photoanode that is isoelectronic to and has a structure similar to $BiVO_4$ can perform as well as a $BiVO_4$ photoanode. Our results indicate that the electron-hole separation efficiency of $PbCrO_4$ is considerably higher than those of most oxide photoanodes and can possibly become as good as that of $BiVO_4$ if its morphology can be further optimized. These results suggest that the electronic and structural similarities of these two compounds are indeed related to their exceptionally high electron-hole separation efficiencies. Their electronic similarities include the presence of filled 6s orbitals of the A-site metal ions (Pb^{2+} and Bi^{3+}) and the empty 3d orbitals of the B-site metal ions (Cr^{6+} and V^{5+}), which interact with oxygen 2p orbitals to constitute the VBM and CBM, respectively. The structural similarities include the coordination environments of the A-site (8-9-fold coordinated polyhedra) and B-site metal ions (4-fold coordinated tetrahedra) that are considerably different from each other, which may effectively suppress the formation of defects where the A-site and B-site ions swap positions. These defects are expected to form more easily in ternary oxides containing two metal ions with similar coordination preferences, which may create interband states that can serve as recombination centers. The CBM of $PbCrO_4$, however, is considerably lower than that of $BiVO_4$ because the 3d orbitals of Cr and V are the major component of the CBM and the 3d orbitals of Cr are energetically lower. This results in the smaller bandgap and more positive E_{FB} of $PbCrO_4$ relative to $BiVO_4$. We found that $PbCrO_4$ is not as photoelectrochemically stable as $BiVO_4$ as a result of differences in redox chemistry and solubility of its constituent metal ions. The similarities and differences between $PbCrO_4$ and $BiVO_4$ elucidated in this study provide new

insights that can be useful in identifying and developing high-performance oxide-based photoanodes.

ASSOCIATED CONTENT

Supporting Information

The Supporting Information is available free of charge on the ACS Publication website:
Additional SEM images, XRD patterns, Mott–Schottky plots, and photocurrent measurements of $PbCrO_4$.

AUTHOR INFORMATION

Corresponding Author

*Email: kschoi@chem.wisc.edu

*Email: gagalli@uchicago.edu

Acknowledgments

We thank Bipul Pandey for useful discussions. This work was supported by the National Science Foundation (NSF) under grant no. CHE-1764399. This research used computational resources of the University of Chicago's Research Computing Center. This research also used resources of the National Energy Research Scientific Computing Center (NERSC), a DOE Office of Science User Facility supported by the Office of Science of the US Department of Energy

References

(1) Walter, M. G.; Warren, E. L.; McKone, J. R.; Boettcher, S. W.; Mi, Q.; Santori, E. A.; Lewis, N. S. Solar Water Splitting Cells. *Chem. Rev.* **2010**, *110*, 6446–6473.

(2) Sivula, K.; van de Krol, R. Semiconducting Materials for Photoelectrochemical Energy Conversion. *Nat. Rev. Mater.* **2016**, *1*, 15010.

(3) Lee, D. K.; Lee, D.; Lumley, M. A.; Choi, K.-S. Progress on Ternary Oxide-Based Photoanodes for Use in Photoelectrochemical Cells for Solar Water Splitting. *Chem. Soc. Rev.* **2019**, *48*, 2126–2157.

(4) Kim, T. W.; Choi, K.-S. Nanoporous $BiVO_4$ Photoanodes with Dual-Layer Oxygen Evolution Catalysts for Solar Water Splitting. *Science* **2014**, *343*, 990–994.
(5) Han, H. S.; Shin, S.; Kim, D. H.; Park, I. J.; Kim, J. S.; Huang, P.; Lee, J.; Cho, I. S.; Zheng, X. Boosting the Solar Water Oxidation Performance of a $BiVO_4$ Photoanode by Crystallographic Orientation Control. *Energy Environ. Sci.* **2018**, *11*, 1299–1306.
(6) Lee, D. K.; Choi, K.-S. Enhancing Long-Term Photostability of $BiVO_4$ Photoanodes for Solar Water Splitting by Tuning Electrolyte Composition. *Nat. Energy* **2018**, *3*, 53–60.
(7) Kudo, A.; Omori, K.; Kato, H. A Novel Aqueous Process for Preparation of Crystal Form-Controlled and Highly Crystalline $BiVO_4$ Powder from Layered Vanadates at Room Temperature and Its Photocatalytic and Photophysical Properties. *J. Am. Chem. Soc.* **1999**, *121*, 11459–11467.
(8) Park, Y.; McDonald, K. J.; Choi, K.-S. Progress in Bismuth Vanadate Photoanodes for Use in Solar Water Oxidation. *Chem. Soc. Rev.* **2013**, *42*, 2321–2337.
(9) Favaro, M.; Uecker, R.; Nappini, S.; Píš, I.; Magnano, E.; Bluhm, H.; van de Krol, R.; Starr, D. E. Chemical, Structural, and Electronic Characterization of the (010) Surface of Single Crystalline Bismuth Vanadate. *J. Phys. Chem. C* **2019**, *123*, 8347–8359.
(10) Cooper, J. K.; Gul, S.; Toma, F. M.; Chen, L.; Liu, Y.-S.; Guo, J.; Ager, J. W.; Yano, J.; Sharp, I. D. Indirect Bandgap and Optical Properties of Monoclinic Bismuth Vanadate. *J. Phys. Chem. C* **2015**, *119*, 2969–2974.
(11) Tachikawa, T.; Ochi, T.; Kobori, Y. Crystal-Face-Dependent Charge Dynamics on a $BiVO_4$ Photocatalyst Revealed by Single-Particle Spectroelectrochemistry. *ACS Catal.* **2016**, *6*, 2250–2256.
(12) Cooper, J. K.; Gul, S.; Toma, F. M.; Chen, L.; Glans, P.-A.; Guo, J.; Ager, J. W.; Yano, J.; Sharp, I. D. Electronic Structure of Monoclinic $BiVO_4$. *Chem. Mater.* **2014**, *26*, 5365–5373.
(13) Kuang, Y.; Jia, Q.; Ma, G.; Hisatomi, T.; Minegishi, T.; Nishiyama, H.; Nakabayashi, M.; Shibata, N.; Yamada, T.; Kudo, A.; Domen, K. Ultrastable Low-Bias Water Splitting Photoanodes via Photocorrosion Inhibition and in Situ Catalyst Regeneration. *Nat. Energy* **2016**, *2*, 16191.
(14) Kim, J. H.; Jang, J.-W.; Jo, Y. H.; Abdi, F. F.; Lee, Y. H.; van de Krol, R.; Lee, J. S. Hetero-Type Dual Photoanodes for Unbiased Solar Water Splitting with Extended Light Harvesting. *Nat. Commun.* **2016**, *7*, 13380.
(15) Sleight, A. W.; Chen, H.-y.; Ferretti, A.; Cox, D. E. Crystal Growth and Structure of BiVO4. *Mater. Res. Bull.* **1979**, *14*, 1571–1581.
(16) Effenberger, H.; Pertlik, F. Four Monazite Type Structures: Comparison of $SrCrO_4$, $SrSeO_4$, $PbCrO_4$ (Crocoite), and $PbSeO_4$. *Zeitschrift fur Krist.* **1986**, *176*, 75–83.
(17) Lee, H. C.; Cho, S. K.; Park, H. S.; Nam, K. M.; Bard, A. J. Visible Light Photoelectrochemical Properties of $PbCrO_4$, Pb_2CrO_5, and Pb_5CrO_8. *J. Phys. Chem. C* **2017**, *121*, 17561–17568.
(18) Cho, S. K.; Akbar, R.; Kang, J.; Lee, W.; Park, H. S. Electrodeposited Single-Crystalline $PbCrO_4$ Microrods for Photoelectrochemical Water Oxidation: Enhancement of Minority Carrier Diffusion. *J. Mater. Chem. A* **2018**, *6*, 13312–13320.
(19) Seabold, J. A.; Choi, K.-S. Efficient and Stable Photo-Oxidation of Water by a Bismuth Vanadate Photoanode Coupled with an Iron Oxyhydroxide Oxygen Evolution Catalyst. *J. Am. Chem. Soc.* **2012**, *134*, 2186–2192.
(20) Govindaraju, G. V.; Wheeler, G. P.; Lee, D.; Choi, K.-S. Methods for Electrochemical

Synthesis and Photoelectrochemical Characterization for Photoelectrodes. *Chem. Mater.* **2017**, *29*, 355–370.
(21) Hohenberg, P.; Kohn, W. Inhomogeneous Electron Gas. *Phys. Rev.* **1964**, *136*, B864–B871.
(22) Kohn, W.; Sham, L. J. Self-Consistent Equations Including Exchange and Correlation Effects. *Phys. Rev.* **1965**, *140*, A1133–A1138.
(23) Perdew, J. P.; Burke, K.; Ernzerhof, M. Generalized Gradient Approximation Made Simple. *Phys. Rev. Lett.* **1996**, *77*, 3865–3868.
(24) Cococcioni, M.; de Gironcoli, S. Linear Response Approach to the Calculation of the Effective Interaction Parameters in the LDA + U Method. *Phys. Rev. B* **2005**, *71*, 35105.
(25) Giannozzi, P.; Andreussi, O.; Brumme, T.; Bunau, O; Nardelli, M.B.; Calandra, M; Car, R.' Cavazzoni, C.; Ceresoli, D.; Cococcioni, M.; Colonna, N.; Carnimeo, I.; Dal Corso, A.; de Gironcoli, S.; Delugas, P.; DiStasio Jr, R.A.; Ferretti, A.; Floris, A.; Fratesi, G.; Fugallo, G.; Gebauer, R.; Gerstmann, U.; Giustino, F.; Gorni, T.; Jia, J.; Kawamura, M.; Ko, H.-Y.; Kokalj, A.; Küçükbenli, E.; Lazzeri, M.; Marsili, M.; Marzari, N.; Mauri, F.; Nguyen, N.L.; Nguyen, H.-V.; Otero-de-la-Roza, A.; Paulatto, L.; Poncé, S.; Rocca, D.; Sabatini, R.; Santra, B.; Schlipf, M.; Seitsonen, A.P.; Smogunov, A.; Timrov, I.; Thonhauser, T.; Umari, P.; Vast, N.; Wu, X.; and Baroni, S. Advanced Capabilities for Materials Modelling with Quantum ESPRESSO. *J. Phys. Condens. Matter* **2017**, *29*, 465901.
(26) Giannozzi, P.; Baroni, S.; Bonini, N.; Calandra, M.; Car, R.; Cavazzoni, C.; Ceresoli, D.; Chiarotti, G. L.; Cococcioni, M.; Dabo, I.; Dal Corso, A.; Fabris, S.; Fratesi, G.; de Gironcoli, S.; Gebauer, R.; Gerstmann, U.; Gougoussis, C.; Kokalj, A.; Lazzeri, M.; Martin-Samos, L.; Marzari, N.; Mauri, F.; Mazzarello, R.; Paolini, S.; Pasquarello, A.; Paulatto, L.; Sbraccia, C.; Scandolo, S.; Sclauzero, G.; Seitsonen, A. P.; Smogunov, A.; Umari, P.; Wentzcovitch, R. M. QUANTUM ESPRESSO: A Modular and Open-Source Software Project for Quantum Simulations of Materials. *J. Phys. Condens. Matter* **2009**, *21*, 395502.
(27) Wang, W.; Strohbeen, P. J.; Lee, D.; Zhou, C.; Kawasaki, J. K.; Choi, K.-S.; Liu, M.; Galli, G. The Role of Surface Oxygen Vacancies in $BiVO_4$. *Chem. Mater.* **2020**, *32*, 2899–2909.
(28) Schlipf, M.; Gygi, F. Optimization Algorithm for the Generation of ONCV Pseudopotentials. *Comput. Phys. Commun.* **2015**, *196*, 36–44.
(29) Hamann, D. R. Optimized Norm-Conserving Vanderbilt Pseudopotentials. *Phys. Rev. B* **2013**, *88*, 85117.
(30) Sun, W.; Ceder, G. Efficient Creation and Convergence of Surface Slabs. *Surf. Sci.* **2013**, *617*, 53–59.
(31) Ong, S. P.; Richards, W. D.; Jain, A.; Hautier, G.; Kocher, M.; Cholia, S.; Gunter, D.; Chevrier, V. L.; Persson, K. A.; Ceder, G. Python Materials Genomics (Pymatgen): A Robust, Open-Source Python Library for Materials Analysis. *Comput. Mater. Sci.* **2013**, *68*, 314–319.
(32) Hjorth Larsen, A.; Jørgen Mortensen, J.; Blomqvist, J.; Castelli, I. E.; Christensen, R.; Dułak, M.; Friis, J.; Groves, M. N.; Hammer, B.; Hargus, C.; Hermes, E.D.; Jennings, P.C.; Bjerre Jensen, P.; Kermode, J.; Kitchin, J.R; Kolsbjerg, E.L.; Kubal, J.; Kaasbjerg, K.; Lysgaard, S.; Bergmann Maronsson, J.; Maxson, T.; Olsen, T.; Pastewka, L; Peterson, A; Rostgaard, C.; Schiøtz, J.; Schütt, O.; Strange, M.; Thygesen, K.S.; Vegge, T.;

Vilhelmsen, L.; Walter, M.; Zeng, Z.; Jacobsen, K.W. The Atomic Simulation Environment—a Python Library for Working with Atoms. *J. Phys. Condens. Matter* **2017**, *29*, 273002.

(33) Mosey, N. J.; Liao, P.; Carter, E. A. Rotationally Invariant Ab Initio Evaluation of Coulomb and Exchange Parameters for DFT + U Calculations. *J. Chem. Phys.* **2008**, *129*, 14103.

(34) Wang, L.; Maxisch, T.; Ceder, G. Oxidation Energies of Transition Metal Oxides within the GGA + U Framework. *Phys. Rev. B* **2006**, *73*, 195107.

(35) Ong, S.P.; Richards, W.D.; Jain, A.; Hautier, G.; Kocher, M.; Cholia, S.; Gunter, D.; Chevrier, V.; Persson, K.A.; Ceder, G. Python Materials Genomics (pymatgen): A Robust, Open-Source Python Library for Materials Analysis. *Computational Materials Science*, **2013**, 68, 314–319.

(36) Freysoldt, C.; Grabowski, B.; Hickel, T.; Neugebauer, J.; Kresse, G.; Janotti, A.; Van de Walle, C. G. First-Principles Calculations for Point Defects in Solids. *Rev. Mod. Phys.* **2014**, *86*, 253–305.

(37) Miseki, Y.; Kitao, O.; Sayama, K. Photocatalytic Water Oxidation over $PbCrO_4$ with 2.3 eV Band Gap in IO_3^-/I^- Redox Mediator under Visible Light. *RSC Adv.* **2015**, *5*, 1452–1455.

(38) Dotan, H.; Sivula, K.; Grätzel, M.; Rothschild, A.; Warren, S. C. Probing the Photoelectrochemical Properties of Hematite (α-Fe_2O_3) Electrodes Using Hydrogen Peroxide as a Hole Scavenger. *Energy Environ. Sci.* **2011**, *4*, 958–964.

(39) Abdi, F. F.; van de Krol, R. Nature and Light Dependence of Bulk Recombination in Co-Pi-Catalyzed $BiVO_4$ Photoanodes. *J. Phys. Chem. C* **2012**, *116*, 9398–9404.

(40) Chen, Z.; Jaramillo, T. F.; Deutsch, T. G.; Kleiman-Shwarsctein, A.; Forman, A. J.; Gaillard, N.; Garland, R.; Takanabe, K.; Heske, C.; Sunkara, M.; McFarland, E.W.; Domen, K.; Miller, E.L.; Turner, J.A.; Dinh, H.N. Accelerating Materials Development for Photoelectrochemical Hydrogen Production: Standards for Methods, Definitions, and Reporting Protocols. *J. Mater. Res.* **2010**, *25*, 3–16. Accelerating Materials Development for Photoelectrochemical Hydrogen Production: Standards for Methods, Definitions, and Reporting Protocols. *J. Mater. Res.* **2010**, *25*, 3–16.

(41) Errandonea, D.; Muñoz, A.; Rodríguez-Hernández, P.; Proctor, J. E.; Sapiña, F.; Bettinelli, M. Theoretical and Experimental Study of the Crystal Structures, Lattice Vibrations, and Band Structures of Monazite-Type $PbCrO_4$, $PbSeO_4$, $SrCrO_4$, and $SrSeO_4$. *Inorg. Chem.* **2015**, *54*, 7524–7535.

(42) Knight, K. S. A Neutron Powder Diffraction Determination of the Thermal Expansion Tensor of Crocoite ($PbCrO_4$) between 60 K and 290 K. *Mineral. Mag.* **1996**, *60*, 963–972.

(43) Setyawan, W.; Curtarolo, S. High-Throughput Electronic Band Structure Calculations: Challenges and Tools. *Comput. Mater. Sci.* **2010**, *49*, 299–312.

(44) Stoltzfus, M. W.; Woodward, P. M.; Seshadri, R.; Klepeis, J.-H.; Bursten, B. Structure and Bonding in $SnWO_4$, $PbWO_4$, and $BiVO_4$: Lone Pairs vs Inert Pairs. *Inorg. Chem.* **2007**, *46*, 3839–3850.

(45) Payne, D. J.; Egdell, R. G.; Walsh, A.; Watson, G. W.; Guo, J.; Glans, P.-A.; Learmonth, T.; Smith, K. E. Electronic Origins of Structural Distortions in Post-Transition Metal Oxides: Experimental and Theoretical Evidence for a Revision of the Lone Pair Model. *Phys. Rev. Lett.* **2006**, *96*, 157403.

(46) Baldereschi, A.; Baroni, S.; Resta, R. Band Offsets in Lattice-Matched Heterojunctions: A

Model and First-Principles Calculations for GaAs/AlAs. *Phys. Rev. Lett.* **1988**, *61*, 734–737.
(47) Bjaalie, L.; Himmetoglu, B.; Weston, L.; Janotti, A.; Van de Walle, C. G. Oxide Interfaces for Novel Electronic Applications. *New J. Phys.* **2014**, *16*, 25005.
(48) Seo, H.; Ping, Y.; Galli, G. Role of Point Defects in Enhancing the Conductivity of $BiVO_4$. *Chem. Mater.* **2018**, *30*, 7793–7802.

TOC Graphic